High temperature oxidation and room temperature axial strength of pre-oxidized zircaloy-4 cladding after a simulated LOCA

Jean Desquines, Christian Duriez, Severine Guilbert, Tatiana Taurines

High temperature oxidation and room temperature axial strength of pre-oxidized Zircaloy-4 cladding after a simulated LOCA

Jean Desquines, Christian Duriez, Séverine Guilbert, Tatiana Taurines

ABSTRACT:

The influence of the nuclear fuel cladding pre-oxidation on post-LOCA quench resistance was experimentally studied and then modeled. Adopting a separate effect approach, quenched high temperature oxidized samples were axially loaded in a mechanical device. The pre-existing oxide layer shows a complex influence that was interpreted and modeled using a simple approach reproducing the main observed phenomena. A new correlation was established to evaluate the oxygen enriched α-phase thickness and the zirconia layer growth is analyzed and modeled. These models and correlations were implemented in a failure prediction model finally compared to experimental results.

KEYWORDS:

LOCA, pre-oxidation, high temperature oxidation, embrittlement

GLOSSARY:

$\alpha(O)$: is the oxygen enriched α-zirconium layer,

BJ: Baker-Just,

CP: Cathcart-Pawel,

Δe_{ox} : increase in the oxide layer thickness during high temperature oxidation,

Δm : sample weight change,

$\left(\frac{\Delta m}{S}\right)_{BJ,CP}$: Baker-Just [BAK62] or Cathcart-Pawel [CAT77] correlations for weight gain normalized by the sample surface exposed to the oxidizing environment,

ECR: Equivalent Clad Reacted,

$e_{\alpha(O)}$: oxygen enriched α layer thickness,

$e_{prior-\beta}$: $prior-\beta$ layer thickness,

e_{ZrO_2}: zirconia layer thickness,

f_α : α-phase fraction in the metal after high temperature oxidation,

LT: Low Temperature, might be used to designate the pre-oxide layer as LT layer,

HT : High Temperature,

$[H]_{prior-\beta}$: $prior-\beta$ layer hydrogen content , assumed to be equal to: $[H]_{prior-\beta} = [H]_{LT+HT}/(1-f_\alpha)$,

$[H]$ LT : hydrogen content of the LT pre-oxidized cladding,

$[H]$ LT+HT : hydrogen content in the metal after HT oxidation of the pre-oxidized material,

LEFM: Linear Elastic Fracture Mechanics,

LOCA: Loss Of Coolant Accident,

m_M: weight of metal in the sample after pre-oxidation and before HT oxidation,

M_O, M_{Zr}: molar weight of oxygen (16 g/mol) and zirconium (91.22 g/mol).

$\aleph(\bar{x};\sigma)$: normal distribution with average value $\bar{x}$ and standard deviation σ.

S: sample surface exposed to high temperature oxidation,

σ_R: fracture axial stress corresponding to the applied load at failure normalized by the gage section of the high temperature oxidized axial tensile sample,

WG: Weight Gain.

Table des matières

1 Introduction

Nuclear fuel claddings are corroded by the coolant water during normal operation. The influence of this pre-existing oxide layer on the cladding oxidation behavior during a LOCA was addressed by several authors [VRT05], [KIM06], [GUI14], [LES19] using laboratory pre-oxidized samples and more recently by Narukawa [NAR19] testing irradiated samples with corrosion layer. The laboratory pre-formed oxide scales were shown in most studies to have a protective influence on further cladding oxidation at elevated temperature and the corrosion induced significant hydrogen pickup during the LOCA. However, Kim [KIM06] observed no influence of pre-existing oxide layer on the high temperature oxidation. The protective influence is mainly observed on the measured weight gain and limits the high temperature oxide scale growth. Recent studies also evidenced that oxide scales formed at high temperature can have a comparable protective influence [LEE16].

Semi-integral thermal shock tests performed first at Mitsubishi Heavy Industries [HON01] and later at JAEA [NAG04, NAG05, NAG06, NAG09, NAG10] were intensively used in France to establish a new LOCA acceptance criteria [BOU15, CAB15] and more recently comparable tests were performed in the EDF laboratories [THI19]. In the JAEA tests, the cladding corrosion was considered to have two main consequences during normal operation: hydrogen uptake in the metal and the cladding wall thickness is slightly reduced due to metal consumption.

IRSN develops a strategy to provide a step by step analysis (using axial tensile samples machined on cladding tubes) of the LOCA semi-integral thermal shock tests developed. Past studies addressed the influence of: i) the hydrogen content [DES16], ii) the two-sided versus one sided oxidation [DES18]. Both aspects were modeled relying on fracture mechanics. These two first studies offered some insight to better understand the competition between on one hand the ballooned, burst and two-sided oxidized region with low hydrogen content, and on the other hand the one-sided oxidized and less deformed region having high hydrogen content (due to secondary hydriding).

In the present study, the high temperature oxidation behavior of pre-oxidized axial tensile specimens is experimentally studied and analyzed using the same approach than the one applied to pre-hydrided bare axial tensile samples [DES16, DES18]. A model continuously describing the high temperature oxidation behavior of as-received bare tubes or pre-oxidized tubes is first proposed. A linear elastic fracture mechanics approach from [DES18] is then expanded to pre-oxidized samples to describe the brittle failure of high temperature oxidized cladding tubes with or without pre-oxidation layers. Using comparable geometries enables comparison between the results of these testing campaigns. Tensile samples were pre-oxidized under a mixture of steam and O_2 and then subjected to a simulated LOCA transient in a vertical furnace under steam environment. The high temperature oxidation was interrupted by a water quench and, after this, the sample was subjected to a mechanical test to check the degree of the material embrittlement. Results are analyzed with the support of the previous oxidation and tensile tests campaigns [DES16, DES18], as well as taking into account the data from previous high temperature oxidation campaigns with pre-oxidized claddings [GUI14, GUI16]. The analyzed data provide a better understanding of possible expectations on irradiated claddings.

2 Experimental

2.1 Materials

Stress Relieved Annealed (SRA) low-tin Zry-4 with nominal chemical composition described in Table 1 was used in this study. The alloy was manufactured by CEZUS. The outer diameter of the tubes is 9.5 mm and the cladding thickness, 0.57 mm.

Table 1. Ingot Measured chemical composition of the tested SRA Zry-4 (Cezus data).

Sn (wt%)	**Fe (wt%)**	**Cr (wt%)**	**O (wt%)**	**H (wppm)**
1.30±0.01	0.22±0.01	0.11±0.01	0.13±0.01	7

2.2 Testing protocol

The testing protocol, rather similar to the one described in [DES16], is illustrated in Figure 1 and was adjusted to an evaluation of the post-quench resistance of a pre-oxidized cladding subjected to a simulated LOCA. The main steps of the protocol are the following:

- Three legs axial tensile samples are first machined using spark machining (Figure 2-a),
- The samples are then pre-oxidized at 470°C in a horizontal furnace under a flowing adjusted mixture of O_2 and steam , leading to two-side oxidation, up to respectively about 30 and 60 µm thick oxide layers,
- Part of the unsymmetrical leg of the pre-oxidized axial samples is cut and hydrogen measurement is performed on this extracted fragment (Figure 1-b),
- The inner side of the remaining unsymmetrical leg is sandblasted and a B-type thermocouple is spot welded. The sample is then further pre-oxidized at 470°C under air during 2 days to avoid any possible overshoot due to fast oxidation at elevated temperature of the bared sandblasted surface. The sample is then weighted (Figure 1-b),
- Centering alumina parts are used for high temperature oxidation (Figure 2-b),
- The sample is positioned under the furnace, the thermocouple wires are connected to B-type thermocouples wires inserted in a hollow alumina rodlet sliding axially within the vertical furnace tube , the sample is centered using alumina parts top and down to hold the sample (Figure 1-c),
- A mixture of over-heated argon and steam is injected by the upper part of the 1100°C or 1200°C heated vertical furnace (Figure 1-c). The furnace temperature profile was determined before testing and a 120 mm long region with less than 2°C temperature gradient was axially located. A high flow rate is used to avoid steam starvation (600 Nl/h argon flow mixed with 500 g/h steam, corresponding to a 50/50 Ar/steam vol. fraction, the steam flow rate normalized to the cross-sectional area of the furnace alumina tube was 19.6 $mg.cm^{-2}.s^{-1}$),
- The sample is then inserted at the maximum temperature region of the furnace during a period chosen to reach a target degree of cladding oxidation,
- The sample oxidation ends by dropping the sample into a 5 liters water bath (Figure 1-c). The cooling rate measured by thermocouples is in the order of 200°C/s. The sample quench temperature was the same as oxidation temperature. The water bath remained below 40°C

after the quench. In this situation no influence of the water bath temperature variation on the sample ductility is expected,

- The sample is extracted from the water bath, dried and weighted,
- The sample is then mounted in an INSTRON 55-67 electromechanical device using pins and tensile tested at room temperature under a constant displacement rate (1mm/min) up to failure to evaluate the degree of material embrittlement,
- Post-test examinations are then performed including optical fractography, eddy current measurements and metallography of cross sections (see Table 2). Thicknesses of the different successive layers (zirconia layers at inner and outer surface, oxygen enriched α(O) layers), prior-β cladding thickness) are accurately determined combining these different techniques. A Keyence VHX-5000 was used for optical characterizations and the measurements are performed with a 1 to 2 µm accuracy using this microscope. Measurements of α(O) and zirconia layer thicknesses rely at least on three measurements on the inner side and three others on the sample outer surface for both metallography and fractography. A Wilson Wolpert WCG-310 magnetic gauge was used with six measurements to determine cumulated thickness of zirconia and α(O) (three on each outer surface legs).

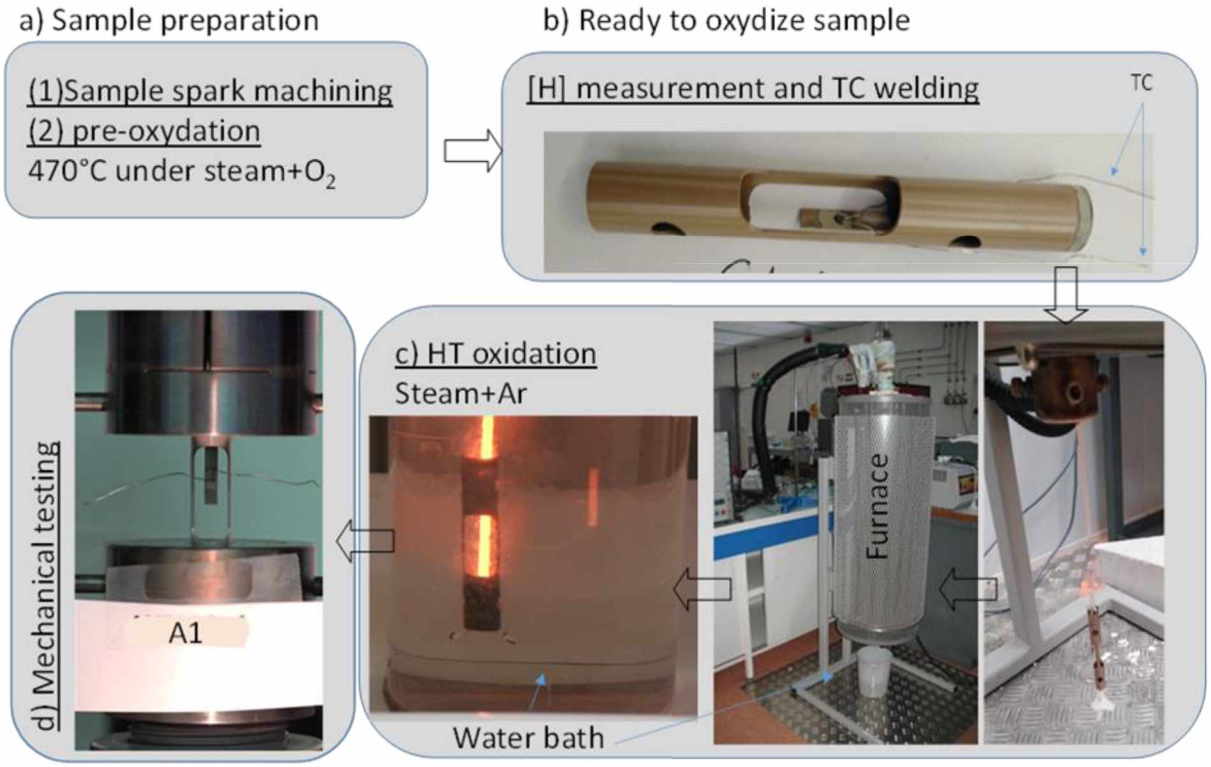

Figure 1: testing protocol to evaluate the influence of cladding pre-oxidation on LOCA post-quench embrittlement (the water bath can be changed, in the present study a 5 liters water bath was used to limit water heating during the quench whereas a borosilicate beaker was used in other programs to visualize the sample quench and the radiation of the hot alumina rodlet during the quench as illustrated here).

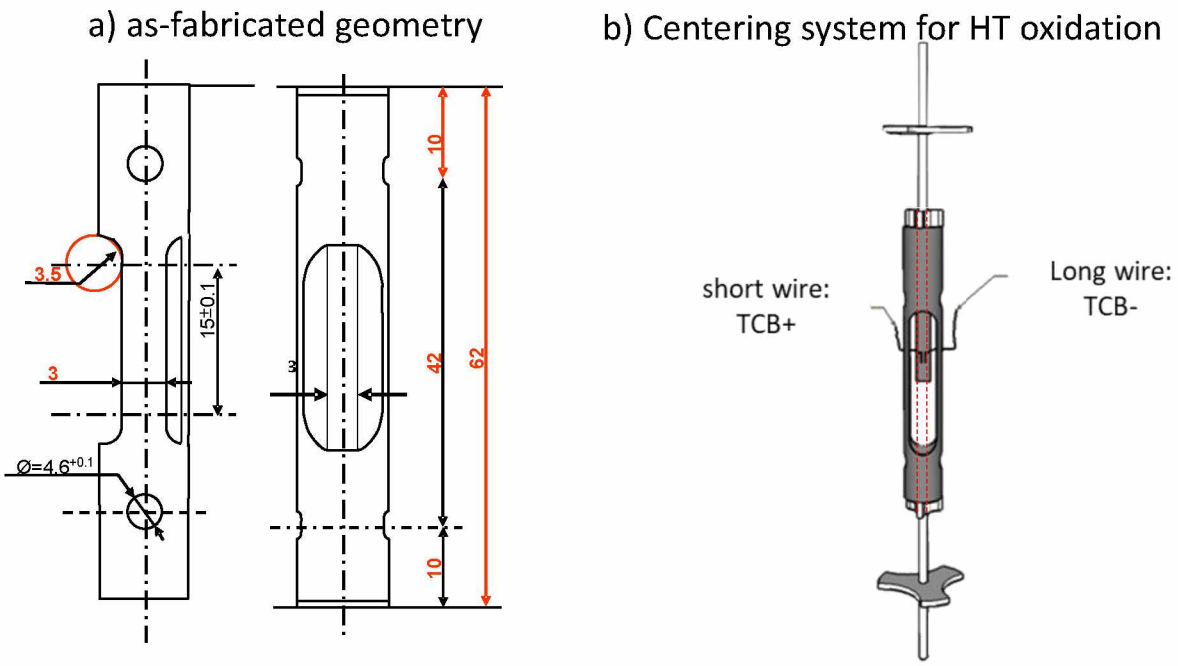

Figure 2: As-machined sample geometry and sample centering system for high temperature oxidation.

Table 2. Post-test examinations

Examination ID	non destructive/*destructive*	measurements
#1	Outer surface visual examination at low magnification (Keyence VHX 5000 optical microscopy)	Check the aspect and color of the outer and inner zirconia layer surfaces
#2	Fractography of the broken surface (Keyence VHX 5000 optical microscopy)	Phase thickness measurements: $\alpha(O)_{internal}$; $\alpha(O)_{external}$; $ZrO_{2_{internal}}$; $ZrO_{2_{external}}$; prior-β-Zr
#6	Magnetic gauge WCG-310 measurement at outer surface	Cumulated thickness: $\alpha(O)_{external}$+$ZrO_{2_{external}}$
#3	Measurement of the sample legs thicknesses	Loaded section of the sample to convert loads into stresses
#4	*Axial-radial metallography of a broken leg*	α(o) internal/external; ZrO_2 internal/external; cladding sample thickness
#5	*Post-oxidation hydrogen content measurement by hot extraction using a LECO ONH-836. A minimum of 6 measurements is performed when possible*	Hydrogen pick-up by difference after – before HT oxidation

#7	*Oxygen radial profile is measured using a CAMECA microprobe*	Average thickness : $\alpha(O)_{average}$

2.3 Test matrix

Thirteen tests were performed, two were oxidized at 1100°C and eleven at 1200°C. Specimens with different pre-oxide layer thickness were tested. Pre-oxide layer thicknesses were about 30 or 60 µm at both inner and outer surface (two-sided oxidation, same inner and outer ZrO_2 thickness). A metallography of the 30 µm thick pre-oxide layer showing the pre-oxide microstructure before high temperature oxidation is shown in Figure 3. The microstructure of the 60 µm thick oxide layer is comparable.

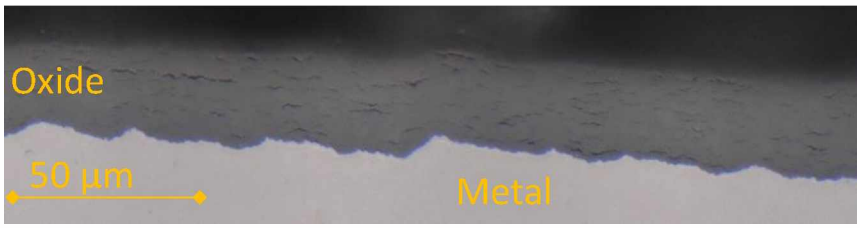

Figure 3: Optical metallography of 30µm thick pre-oxide layer.

The temperature measured by the thermocouple was recorded during each test and an equivalent isothermal oxidation condition was evaluated as follows (designated as average temperature in Table 3): The Cathcart-Pawel [CAT77] correlation for α(O) layer thickness was used to determine the α(O) layer thickness increase at each temperature step using the thermocouple measurement record and then an equivalent isothermal temperature and oxidation duration were determined as a compromise leading to a minimum variation between the measured temperature and the calculated isothermal average temperature (cf. Table 3). The calculation of isothermal parameters is detailed in the appendix. This procedure is necessary because the measurements showed that the presence of pre-oxide induced a significant slower temperature increase compared to as-received bare cladding samples subjected to high temperature oxidation. The α(O) layer thickness is used to determine the equivalent temperature because it is expected that this parameter is not strongly influenced by a pre-existing oxide layer, indeed this layer is an oxygen source and this assumption will be later verified by analyzing existing data. Exothermal oxidation induces a faster temperature increase when testing bare samples than pre-oxidized samples. The uncertainty on the equivalent isothermal oxidation temperature (see appendix) is mainly linked to recorded temperature variations of 10 to 30°C above and below this equivalent temperature between the beginning of effective oxidation period (mentioned as t_i, in the appendix) and the sample quench (mentioned as t_f, in the appendix). This uncertainty is significantly larger than the thermocouple measurement accuracy (about 5°C) and can be considered as the main cause for uncertainty on the equivalent temperature value.

The ECR parameter is unambiguously defined for bare samples as the mass-fraction of high temperature oxidized cladding material but this concept has to be clarified for pre-oxidized samples.

Here, we define the ECR as the ratio of the mass of metal oxidized at high temperature to the mass of metal in the sample after pre-oxidation (m_M) :

$$ECR_{HT} = \frac{\Delta m}{\frac{2.M_O}{M_{Zr}} m_M} \qquad (1)$$

Therefore, the metal converted into oxide during the pre-oxidation phase is not included in the calculation. Only the metal consumed at high temperature is considered, as indicated by the HT subscript.

This ECR_{HT} parameter can thus be evaluated directly from the weight gained during the high temperature phase, either using a measured value or values from pre-existing correlations such as Baker-Just [BAK62] or Cathcart-Pawel [CAT77], $\left(\frac{\Delta m}{S}\right)_{BJ,CP}$. This leads to the following modified evaluation of this parameter depending on the surface, S, exposed to high temperature oxidation: $ECR_{BJ,CP} = \frac{\left(\frac{\Delta m}{S}\right)_{BJ,CP}.S}{\frac{2.M_O}{M_{Zr}}m_M}$. Table 3 indicates the Equivalent Clad Reacted (ECR) evaluated using Baker-Just correlation [BAK62]. The Baker-Just and Cathcart-Pawel evaluations are affected by equivalent temperature uncertainty whereas the measured weight gain is extremely accurate. Their variation bounds are calculated within the temperature uncertainty range in the following tables.

Table 3. High temperature oxidation test matrix on pre-oxidized samples (*: corresponds to axial tensile samples that failed at pin location and cannot be used to evaluate the mechanical resistance of the samples, **: calculated according appendix)

Test ID	*Pre-oxide layer thickness*	*Average oxidation temperature***	*Maximum temperature variation***	*Oxidation duration*	*Baker-Just ECR*
(#)	*(µm)*	*(°C)*	*(°C)*	*(s)*	*(%)*
A-1	30	1182	29	179	$17.7^{+2.9}_{-2.6}$
A-2		1198	27	184	$19.3^{+2.9}_{-2.6}$
A-3*		1194	23	160	$17.9^{+2.3}_{-2.1}$
A-4		1192	28	134	$16.1^{+2.5}_{-2.3}$
A-5		1192	35	104	$14.2^{+2.8}_{-2.5}$
A-6		1190	31	78	$12.2^{+2.2}_{-1.9}$
A-12		1200	18	131	$16.7^{+1.6}_{-1.5}$
A-7*	60	1189	25	102	$15.0^{+2.1}_{-1.9}$
A-8		1186	36	82	$13.1^{+2.7}_{-2.4}$
A-9*		1185	24	89	$13.6^{+1.9}_{-1.7}$
A-10		1191	15	95	$14.6^{+1.2}_{-1.1}$
A-11	30	1094	11	472	$17.3^{+1.2}_{-1.1}$
A-13		1093	13	346	$14.7^{+1.2}_{-1.1}$

Due to the combined oxygen and hydrogen embrittlement three samples failed at the pin loading hole. However, these test results can be partly used to address some issues different from cladding embrittlement.

3 High temperature oxidation results

3.1 Summary of the main results

The main results addressing samples oxidation are summarized in Table 4. The oxide layer thickness values mentioned in this table are the average values of inner and outer surfaces measured using metallography analysis.

Table 4. Main results to analyze oxidation behavior of pre-oxidized samples (*: samples that failed at pin loading holes - n.m.: not measured - [H] is hydrogen content - the two last greyed lines correspond to 1100°C oxidation, all other specimens were oxidized at 1200°C – one standard deviation uncertainties are provided for $e_{ZrO_2,LT+HT}$ and $e_{\alpha(O)}$ measurements).

Test ID	CP-ECR	WG based ECR_{HT}	$e_{ZrO_2,LT}$	$[H]_{LT}$	$e_{ZrO_2,LT+HT}$	$e_{prior-\beta}$	$e_{\alpha(O)}$	$[H]_{LT+HT}$
(#)	(%)	(%)	(µm)	(wppm)	(µm)	(µm)	(µm)	(wppm)
A_1	$13.8^{+2.0}_{-1.8}$	5.15	29	172	38.4±2.0	442	40.1±1.0	311
A_2	$14.9^{+2.0}_{-1.8}$	7.71	29	n.m.	47.0±2.0	413	53.9±1.4	281
A_3*	$13.8^{+1.5}_{-1.4}$	7.79	29	173	45.6±2.9	411	45.2±0.9	224
A_4	$12.5^{+1.7}_{-1.6}$	5.97	27	156	40.8±1.9	423	43.8±1.3	216
A_5	$11.0^{+1.9}_{-1.7}$	4.25	27	145	35.9±1.4	449	37.1±1.5	236
A_6	$9.50^{+1.5}_{-1.3}$	3.23	31	170	35.8±2.1	463	33.0±1.0	287
A_12	$12.9^{+1.1}_{-1.0}$	0.17	30	172	67.7±3.4	424	35.4±1.2	278
A_7*	$11.6^{+1.4}_{-1.3}$	3.42	60	328	63.4±2.1	407	32.0±1.3	509
A_8	$10.2^{+1.8}_{-1.6}$	2.8	59	320	65.8±2.0	425	31.4±1.2	489
A_9*	$10.6^{+1.3}_{-1.2}$	3.02	59	345	68.9±1.5	418	39.1±2.0	534
A_10	$11.3^{+0.8}_{-0.8}$	3.73	61	318	28.3±1.3	405	53.6±1.2	551
A_11	$14.4^{+0.9}_{-0.8}$	3.73	30	180	42.2±1.4	429	44.0±1.5	632
A_13	$12.3^{+0.9}_{-0.8}$	2.57	30	179	28.5±1.5	444	44.4±1.5	466

ECR measurements after 1200°C oxidation are plotted in Figure 4. The Baker-Just correlation leads, as expected from the weight gain correlations, to 30% higher ECR_{HT} than the Cathcart-Pawel correlation. For bare Zircaloy-4 oxidized at 1200°C, the Baker-Just is considered as a conservative evaluation of the ECR_{HT} derived from weight gain and the Cathcart-Pawel correlation is expected to provide a rather accurate evaluation of this value. The ECR_{HT} derived from weight measurement of pre-oxidized samples is significantly lower than the CP-ECR. This evidences a protective influence of pre-oxidation regarding weight-gain. The measured ECR_{HT} for 30 µm and 60 µm are almost comparable except for one outlying ECR_{HT} value close to 0 associated to sample A_12 (see Table.4). The table 4 shows that at 1100°C and 1200°C the protective influence of a pre-oxide scale appears stronger in terms of weight gains or oxide layer growth at high temperature.

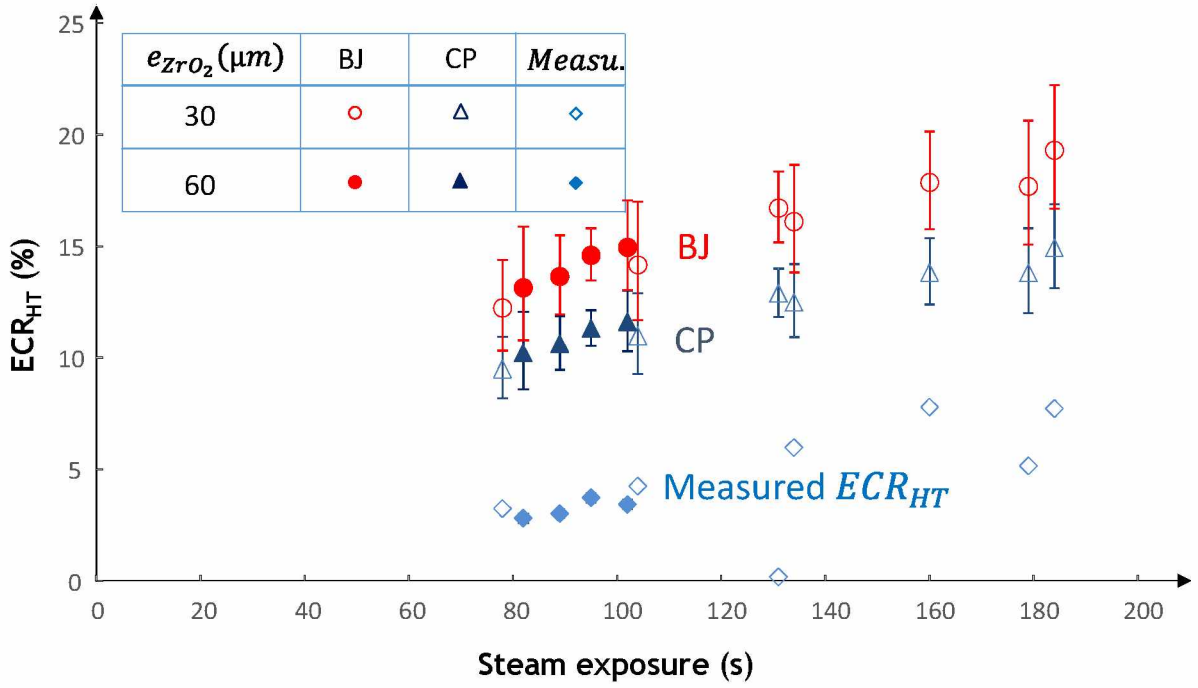

Figure 4: Comparison of ECR assessment after 1200°C high temperature oxidation using: weight gain measurements, Cathcart-Pawel and Baker-Just correlations.

3.2 Post-test examinations

3.2.1 Surface examination

Figure 5 shows the outer surface visual aspect of the axial tensile samples at a broken leg. Dark patches separated by two approximatively orthogonal networks of cracks are always visible and more clearly on 30 µm pre-oxidized samples. The dark patches correspond to substoichiometric oxide [MAK76, BRA12]. Here, the initially bright and stoichiometric pre-oxide scale has been chemically reduced up to its outer surface, due to the strong affinity of the metal for oxygen: during the high temperature transient, oxygen is transferred from the oxide to the metal and forms the oxygen-enriched α(O) layer. The pre-oxide scale is interspersed with cracks perpendicular to its surface, and here the metal "pumping" effect is compensated by oxygen exchange with the atmosphere, as it has been evidenced by oxidation experiments using isotopically-marked oxygen 18 gas [KAS18]. Therefore, the oxide keeps in the vicinity of cracks its stoichiometry and its initial bright color. The stoichiometric oxide is not only located in the vicinity of the crack but extend laterally due to the contribution of lateral cracks defining the layered structure of the pre-oxide scale. On cross sections (see Figures 6 and 7), when observed in polarized light illumination, the stoichiometric oxide regions are visible as bright patches having a more or less triangular shape (cf. Figure 8, see test A12 were a detailed view of bright oxide is included, note that the vertical cracks networks may have been created during the pre-oxidation phase or/and during the high temperature phase).

It is worthwhile noticing that compared to the 30 µm pre-oxidized samples, the regions of bright oxide are laterally much more extended than for the 60 µm pre-oxidized specimens. It is expected that

because of the larger metal to oxide surface distance, the metal influence is less effective at the oxide surface, which therefore tends to remain equilibrated with the atmosphere.

At the sample machined legs edges (see Figure 5 and Figure 6), the oxide surface appears brighter than elsewhere. This is specifically obvious at 1100°C (see Figure 6). Metallographic cross sections or fractography reveal that close to the edges, the high temperature oxide thickness is significantly higher than away from the edges (Figure 7). Two effects are expected at the edges: an early loss of the pre-oxide protective influence [DUR19] and a more disorganized high temperature oxide due to the geometrical singularities. One may establish a link between this edge effect, obviously stronger at 1100°C than at 1200°C, and the stronger hydrogen pick-up during the high temperature phase observed for the tests at 1100°C.

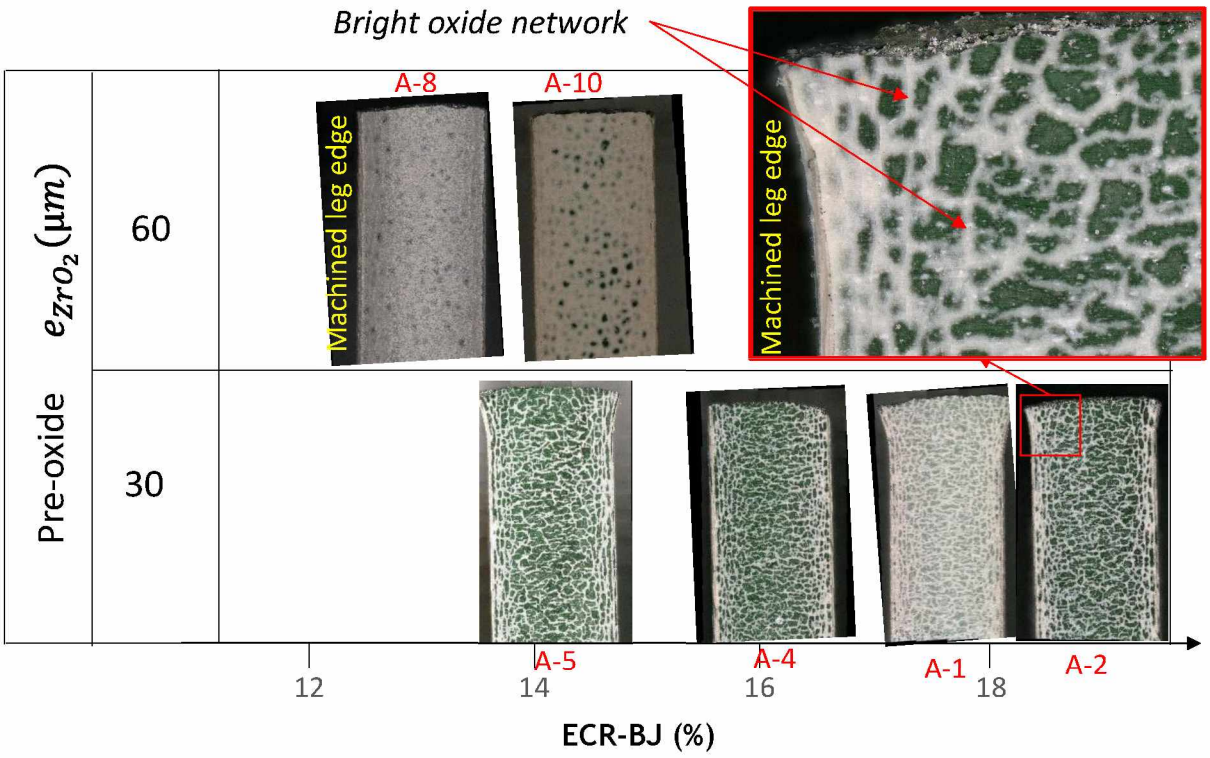

Figure 5: Outer surface visual examination of the samples broken leg after oxidation at 1200°C.

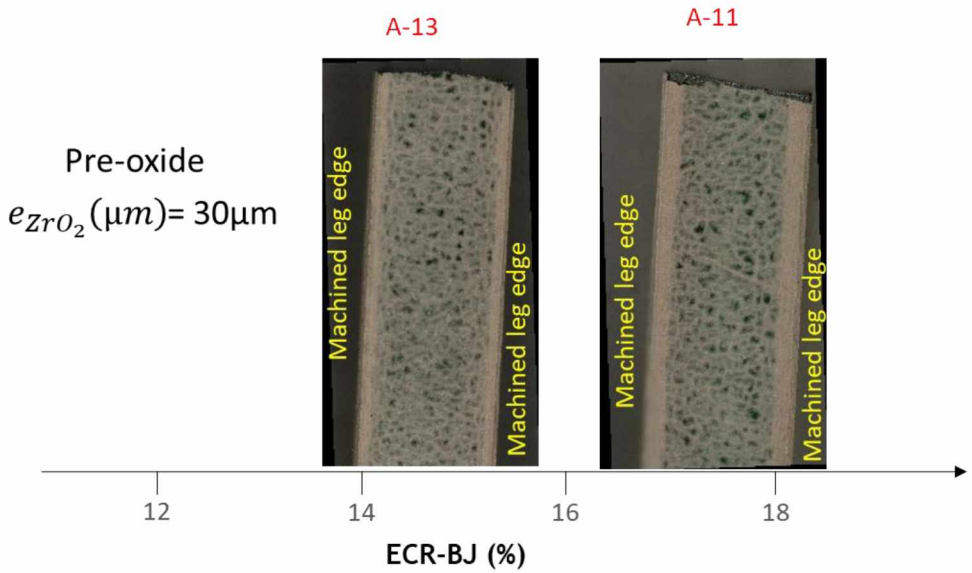

Figure 6: Outer surface visual examination of the samples broken leg after oxidation at 1100°C.

3.2.2 Hydrogen pickup during high temperature oxidation

The sample hydrogen content was measured before and after the high temperature phase by hot extraction (see Table 4). The uncertainty of the measurement is mainly due to the uncertainty on hydrogen content of the standards used, corresponding to about 5 to 10% of the measured hydrogen content. Some hydrogen pickup was evidenced during high temperature oxidation, this is most probably related to the microstructure of the pre-oxide layer. The hydrogen pickup appears stronger for 1100° (tests A-11 and A-13) than for 1200°C oxidation temperature. The hydrogen pickup seems not to be only related to the weight gain-based ECR, and it is believed that most of the hydrogen pickup occurs at machined leg edges, where HT oxide growths locally faster at regions with bright oxide (see Figure 6 for illustration). Using the diffusion coefficients determined by M. Große [GRO12], the diffusion distance at 1100°C for hydrogen during 100s is much longer than the sample leg half width. In any case, the hydrogen content after high temperature oxidation is assumed to be homogeneous in the sample's legs and is used as an input parameter to interpret the mechanical test results.

3.2.3 Fractography

The fractography was systematically performed using polarized light illumination, and with the facture surface oriented in the (r, θ plane) of the tubes. As an illustration, the fractography of the A-13 broken section is illustrated in Figure 7 .

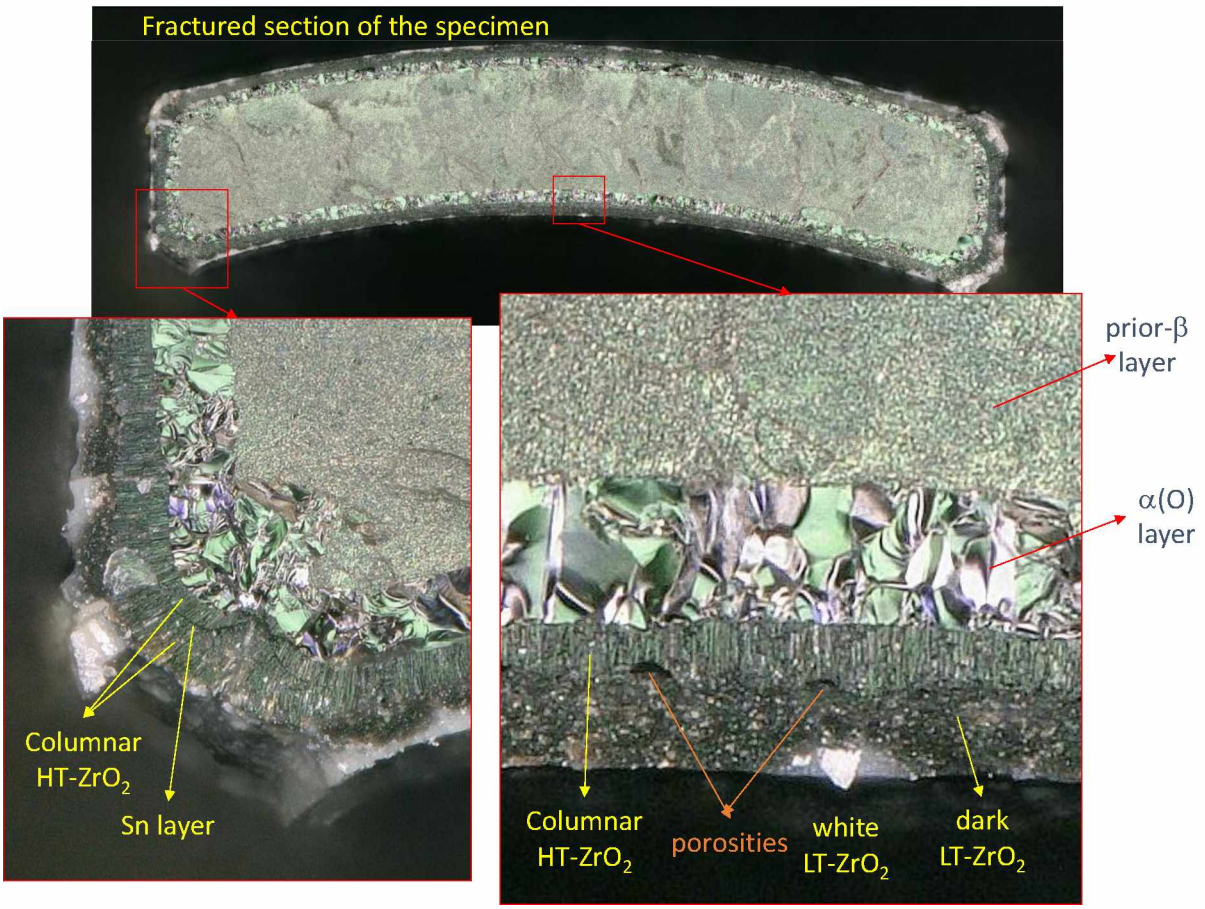

Figure 7: Fractography of A-13 broken leg section.

There are several features of interest visible on this image. The oxide layer is constituted of a set of different layers:

- The remaining pre-oxide appears mostly rather dark except at some localized regions connected to the outer surface, were small lenses of white oxide can be observed. This layer is brittle and its mechanical resistance cannot be differentiated with the one of the high temperature oxide in the present study,

- Between the metal and the remaining pre-oxide layer, a columnar and rather bright high temperature oxide layer has formed. The columnar grains fail by brittle intergranular fracture revealing the columnar microstructure of the grains. This columnar oxide layer is thicker at sample edges and sometimes a tin-rich thin layer can be observed at about mid-thickness of the layer,

- Between the pre-oxide layer and the high temperature oxide layer some regularly spaced interface cracks or porosities can be observed,

- The outer-most layer in the metallic section appears as brittle and bright and corresponds without doubt to the oxygen rich α(O) layer. This layer has an extremely brittle aspect like broken glass resulting from cleavage of large α grains.

- At the central region of the metal, the prior-β layer appears as a rather dull region. The frontier between this prior-β layer and the α(O) layer can be accurately localized within the sample section. The prior-β phase is the load-bearing phase. High resolution micrographs reveal ductile features on

the fracture surface [BRA08, THI19] this might explain the blurry aspect of the surface after optical fractography.

As illustrated in Figure 7 the fractography can be used to identify and measure the different existing layers thicknesses.

3.2.4 Metallography

The metallographic cross sections are prepared in the axial-radial plane of the sample leg, far from leg edges (affected by accelerated oxidation in some samples). The metallography can reveal comparable features to fractography, as illustrated in Figure 8 and Figure 9. For the magnification used in these figures, there is probably less contrast between the different regions than for fractography. However, the porosity line separating the high temperature columnar oxide and the remaining pre-oxide layer is rather clearly observed. The use of polarized light illumination (green-colored images) allows to evidence the bright oxide regions associated with the radial cracks interspersing the pre-oxide scale.

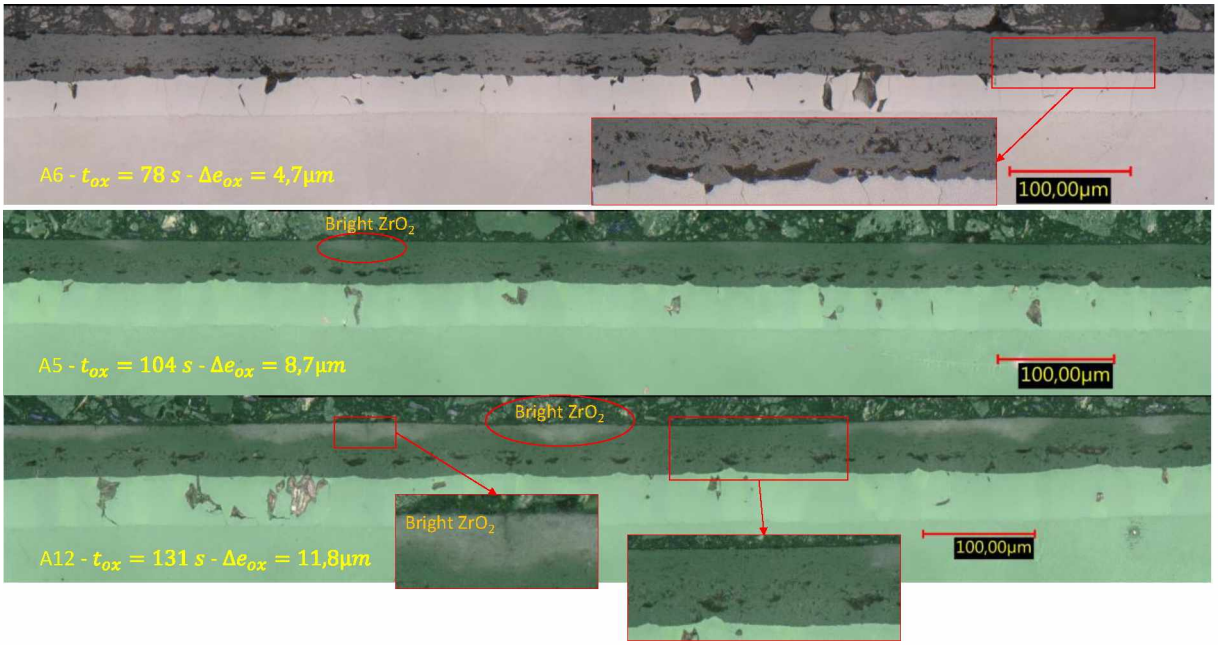

Figure 8: Metallographs under bright field illumination (A-6) and polarized light illumination (A-5 and A12) for samples having a 30 µm thick pre-oxide layer.

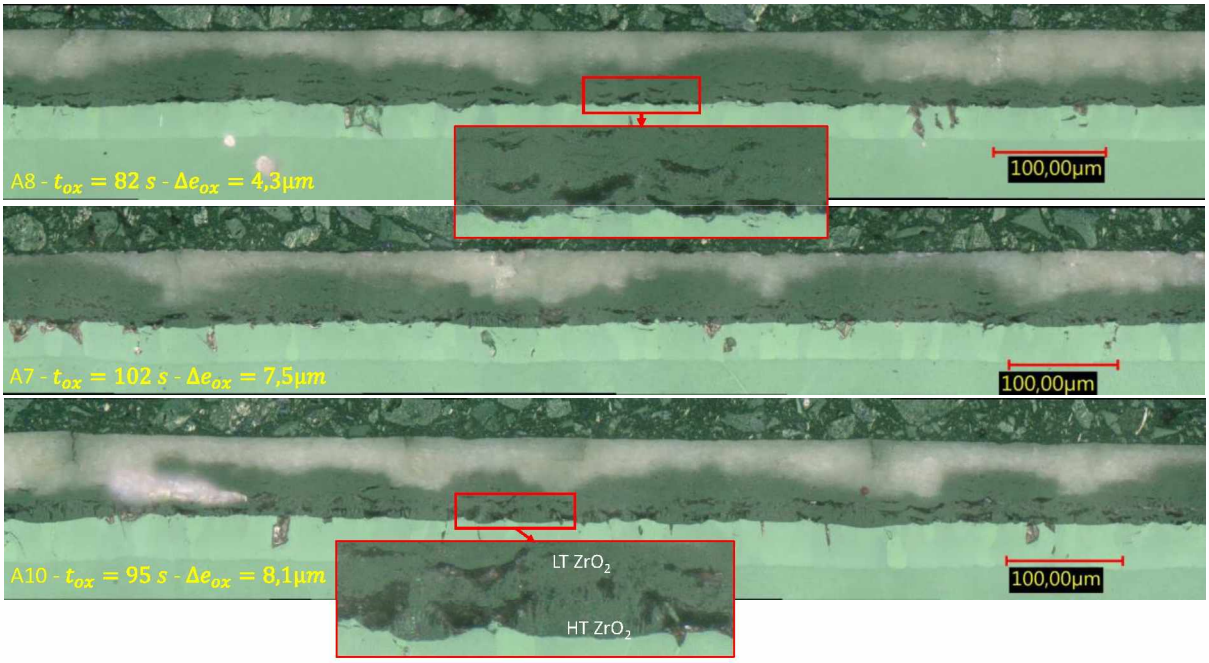

Figure 9: Metallographs under polarized light illumination for samples having a 60 µm thick pre-oxide layer.

3.3 α(O) and ZrO_2 thickness measurements

Measuring the α(O) layer thickness is sometimes a difficult task. In this section, the various thickness measurements techniques used in this study are compared.

3.3.1 Cumulated α(O) and ZrO_2 thickness

The cumulated thickness of α(O) and zirconia layers is determined by three possible measurements: fractography, metallography and magnetic gauge measurements that are compared in Figure 10. All three measurements are consistent together. The magnetic gauge is a non-destructive technique and provides an accurate assessment of the cumulated thickness of these two layers confirmed by both metallography and fractography. A few measurements performed apart from this study indicated that the magnetic gauge was not affected by the presence of 20% α(O) inclusions embedded within the prior-β phase. Measuring the α(O) on the metallography may depend somewhat on the polishing process, while this is not the case for measuring the zirconia layer thickness. Consequently, it might be recommended to combine magnetic gauge measurement and metallography, to assess the zirconia and α(O) layers thicknesses.

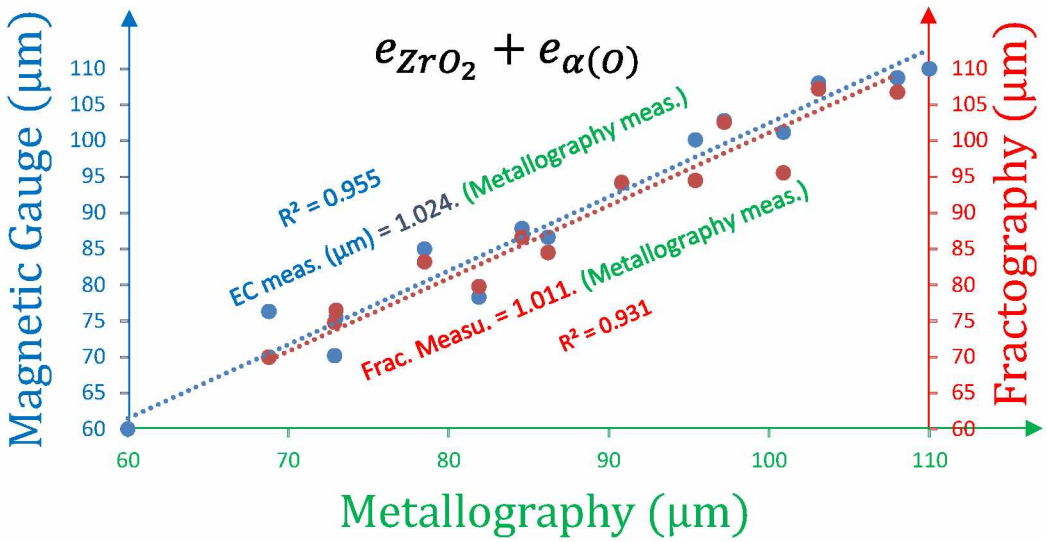

Figure 10: Comparison of three different measurements for the cumulated thickness of α(O) and zirconia.

Few microprobe oxygen concentration profile measurements through the cladding wall thickness were performed on selected specimens. They confirmed that the α(O) layer thickness measurements on metallography and fractography can be considered as accurate.

3.3.2 Total ZrO_2 thickness

The zirconia layer thickness measured by fractography and metallography are compared in Figure 11. The results compare well but the fractographic measurement lead to slightly higher zirconia layer thickness. The measurements performed on the fractography are slightly affected by increased oxidation kinetics close to the sample edges (see Figure 7) whereas the metallography is less affected because performed as far as possible from sample edges.

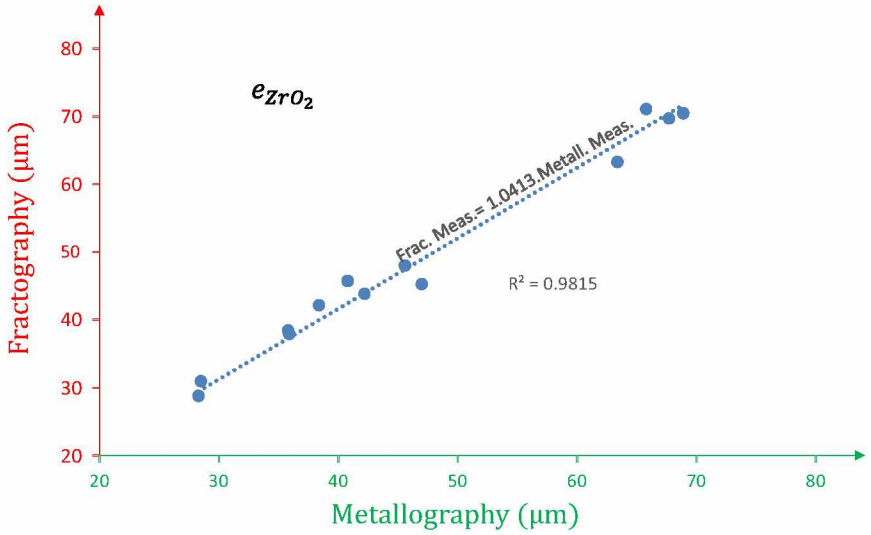

Figure 11: Comparison of two different measurements for the zirconia layer thickness.

4 Reconstructed mechanism for high temperature oxide growth

The combination of the different post-test examinations enables a better understanding of the oxidation process and evidences some of the phenomena inducing a protective influence of a pre-existing oxide layer, as schematically described in Figure 12. The process is divided in some key steps that can be observed on metallographs.

Before high temperature oxidation the pre-oxide layer has regularly spaced piled thin porosities and the pilings are separated by dense zirconia also called veins [BOS06]. However, there are some differences in the morphology of laboratory formed pre-oxides and in-service corrosion layers but this is out of the scope of the present study.

The first steps of the process can be inferred from metallographic images of samples having a very thin HT oxide layer, like in the A-6 test. Here, regularly spaced interfacial pores/cracks are clearly formed between the metal and the pre-oxide layer. Detailed examinations at high magnification show that these pores have a metallic surface and a zirconia surface (see detail of test A6 in Figure 8 or A8 in Figure 9).

At the beginning of the high temperature phase, the outer regions of the pre-oxide layer remains almost stoichiometric and oxygen supply from the outer environment is not facilitated. Therefore, oxygen extracted from the oxide layer by transport/diffusion to the metal is not replaced. Chemical reduction of the oxide thus occurs at the interfacial region, and further reduction leads to ZrO_2 to α(O) conversion. Due to the Pilling-Bedworth ratio, 56% of the oxide volume is converted into void and consequently pore opening can occur. The pores can be seen as a precursor state of oxide delamination and it can be inferred that they act as a barrier to oxidizing species or at least that oxygen transport to the metal will be drastically reduced there. Between the pores, bridges connecting the pre-oxide layer to the metal are observed. These bridges appear as preferential sites for HT oxide formation (step 2 in Figure 12), and at incipient stage of high temperature oxide layer growth, lenticular-shaped HT oxide nodules form there, like for A-6 test. In other terms, it means that at high temperature, the preferential oxygen transport mechanism through the pre-oxide layer is solid state diffusion rather than gas phase mass transport.

Later on, vacancies reach the outer surface, and a stoichiometry gradient is established across the remaining pre-oxide layer, and oxidizing species from the gaseous environment can then be transported through the oxide layer for high temperature oxidation of the metal. Afterwards, HT oxide develops starting from bridges and simultaneously penetrating into the metal and oxidizing the metallic surface of the opened pores (step 3) the HT oxide layer can then develop as a rather uniform layer toward the metal (step 4).

Consequently, this complex process is expected to induce a delay between the beginning of the high temperature phase and the beginning of the high temperature oxide formation. During this period, the oxygen supplied to the metal by the pre-oxide layer forms the oxygen enriched α(O) layer, that clearly appears in Figure 8 and Figure 9. The pore formation and opening process in the vicinity of the metal-oxide interface can be interpreted as a result of the pre-oxide layer chemical reduction when the metal absorbs oxygen. After formation of the HT oxide nodules, a more continuous layer of columnar oxide free of any pores develops. This layer likely has the same oxygen transport properties than the one formed on a bare Zircaloy surface at the same temperature. However, the remaining pre-oxide layer

might reduce the oxygen supply for the growth of the high temperature zirconia layer. When considering the 60 µm thick pre-oxide layer (Figure 9), a comparable process is observed.

The results observed in the present study are consistent with the statements made in a previous work [GUI14].

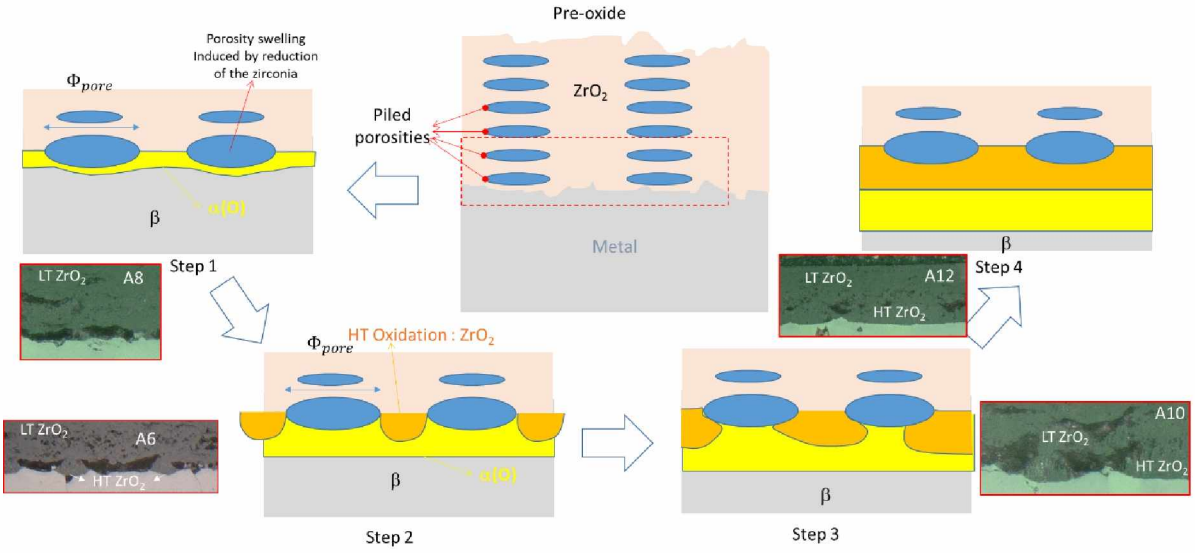

Figure 12: Main steps of the high temperature oxidation process of laboratory pre-oxidized samples

5 α(O) and ZrO_2 thickness modeling

The sample failure is in some situations controlled by linear elastic fracture mechanics (LEFM) [DES16, DES18]. The cracks depth in past modeling was shown to correspond to the cumulated depth of oxide layer thickness and α(O) layer depth. These layers have to be modeled for LEFM assessment this will be discussed later on. The results, completed with data extracted from previous studies are analyzed. Correlations that can be used to model the layers growth kinetics are derived.

5.1 The α(O) layer

The α(O) layer thickness measurements performed in this study are gathered with other sets of measurements obtained in previous studies using optical microscopy, on pre-oxidized as well as on as-received Zircaloy-4 samples ([GUI14, DES16, GUI16]) and compared in Figure 13 to two correlations:

- the Cathcart-Pawel correlation for the α(O) layer thickness [7]:

$$e_{\alpha(O)}(\mu m) = 10000.\sqrt{1.523.e^{-\frac{48140}{1.981.T(K)}}.t(s)} \qquad (2)$$

- a correlation adjusted to the experimental data of the present paper at 1200°C:

$$e_{\alpha(O)}(\mu m) = \sqrt{16.2.t(s)} \qquad (3)$$

To obtain accurate optical microscopy measurements, it was observed that the sample preparation and polishing sequence is a key issue requiring trial and error procedure. The oxygen enriched α-layer is mainly restituted by polishing due to the hardening effect of the oxygen and, close to the α(O)/prior-β interface, this contrast (resulting from the difference in equilibrium concentration in each phase) is not very pronounced even at 1200°C. When decreasing the oxidation temperature, checking the Zircaloy-4-O pseudo-binary phase diagram [CHU77], there is less difference between the oxygen concentration in the α-phase and the β-phase, therefore less contrast is expected at the interface between the two layers. Consequently, the α(O) layer thickness measurement may be affected by increasing uncertainty by decreasing oxidation temperature. The resulting uncertainty is stronger below 1000°C than the one obtained in the Zy-4 β-range. The first outcome of Figure 13 is the good consistency between the as-received bare samples and the laboratory pre-oxidized samples. In other words, there is a negligible influence of the pre-oxide layer on the α(O) layer thickness. Additionally, no influence of hydrogen content was observed in [DES16] between 11 and 4000 wppm on this layer thickness. The α(O) layer thickness has to be considered as an important parameter to interpret complex results on pre-oxidized material because it mainly depends on temperature history at high temperature. This layer thickness might be used to interpret, using metallography, the thermal transient imposed to cladding tubes. For example, azimuthal changes in the thickness of this layer can be used to quantitatively determine any temperature gradient.

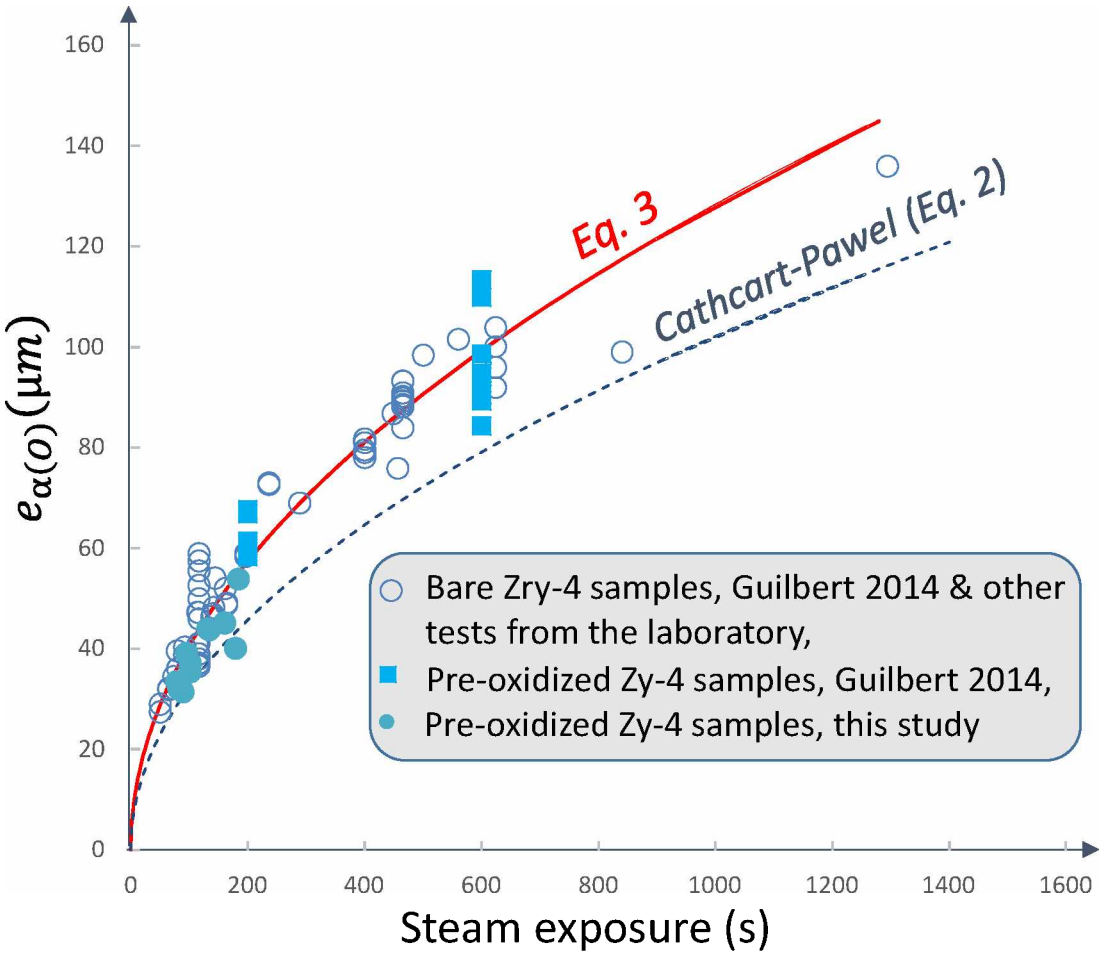

Figure 13: Comparison of the obtained measurements to Cathcart-Pawel correlation at 1200°C.

It clearly appears in Figure 13 that the Cathcart-Pawel correlation for α(O) strongly underestimates the thickness of the α(O) layer. It is rather recommended to use of the eq(2) correlation, applicable at 1200°C. It is suggested that the underestimation of the Cathcart-Pawel correlation for the α(O) layer thickness can be linked to the polishing process used at that time. To check this correlation accuracy, several measurement techniques were crossed-compared in this paper to provide as accurate as possible α(O) layer thickness measurements.

Starting from this statement, it was decided to reanalyze the measurements performed at different steam oxidation temperatures in the laboratory and the ones from Sawarn [SAW16]. The results are plotted in Figure 14 in a Log-Log representation. The measurement appears to significantly deviate from the prediction of the Cathcart-Pawel correlation at each of the tested temperature but also from Urbanic Correlation [URB78].

Therefore, the following equation is proposed, correlating reasonably well all measurements from our laboratory as well as recent data from [SAW16]:

$$e_{\alpha(O)}(\mu m) = e^{\aleph(0;0.1)}\sqrt{K.t(s)} \text{ with: } K = 3.78.10^7.e^{-\frac{21557}{T(K)}} (\mu m^2/s) \qquad (4)$$

$e^{\aleph(0;0.1)}$: describes the uncertainty on the α(O) layer thickness evaluation between 1000 and 1200°C.

The proposed correlation was found to be very close to the one provided by Leistikov [LEI87], well within uncertainty range.

At 900°C, because of the large scatter on the measurements, it is not clear whether the evolution of the α phase follows a parabolic or cubic evolution with time, as suggested by Cathcart-Pawel [CAT77]. Close to the α-β transition temperature the scatter is so large that model predictions are not accurate. This might result from the reduced difference in oxygen composition between these two phases leading to a less contrasted α(O) layer after metallographic preparation of the samples.

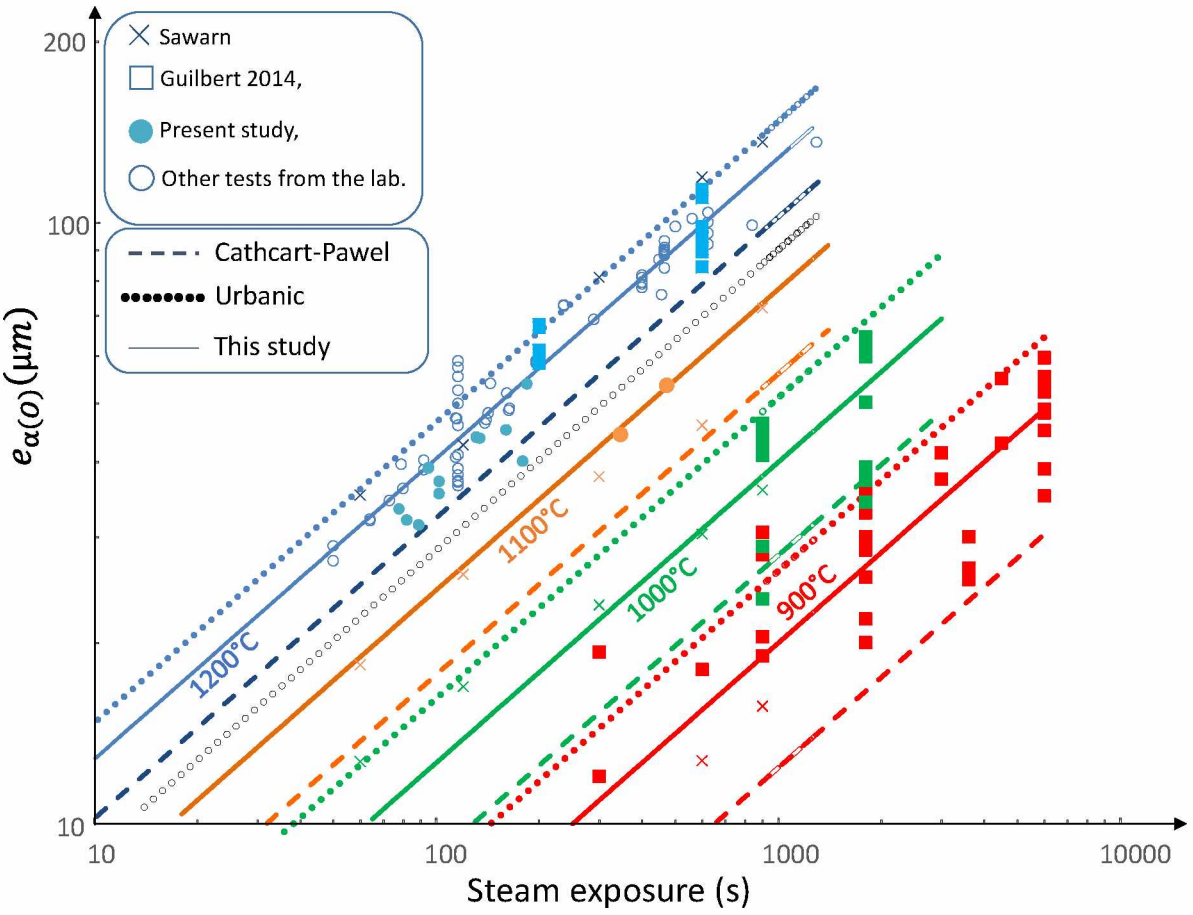

Figure 14: α(O) layer thickness experimental measurements compared to the Cathcart-Pawel and Urbanic correlations and to the proposed parabolic correlation (eq. (4)).

5.2 High temperature oxide growth kinetics

On the basis of the discussion on the growth mechanism of the high temperature oxide that forms at 1200°C under the pre-oxide (see section 4), one can suggest a simple modeling for the oxide layer growth:

$$\Delta e_{ox}(\mu m) = \delta(\mu m) + [K(t - t_D)]^{1/n} \quad (5)$$

Δe_{ox} is the thickness of the high temperature oxide layer formed at time t

$\delta(\mu m)$: is the irreversible growth of the scale induced by the swelling of the porosities in the vicinity of the oxide-metal interface.

t_D : is a delay to initiate uniform high temperature oxidation (step 4 in Figure 12).

K : is a kinetic constant affected by the presence of the pre-oxide. The pre-oxide acts as a filter limiting the oxidizing species supply at the interface between the remaining pre-oxide and the high temperature oxide.

Using all the data available during the present experimental program but also during the Guilbert's test program [GUI14], equation 5 was adjusted on the data and plotted in Figure 15. There is a reasonable agreement between the proposed model and the experimental data. But, including additional experimental data would clearly contribute to a better validation of this model. A follow up study with lower pre-transient oxide thicknesses would be interesting.

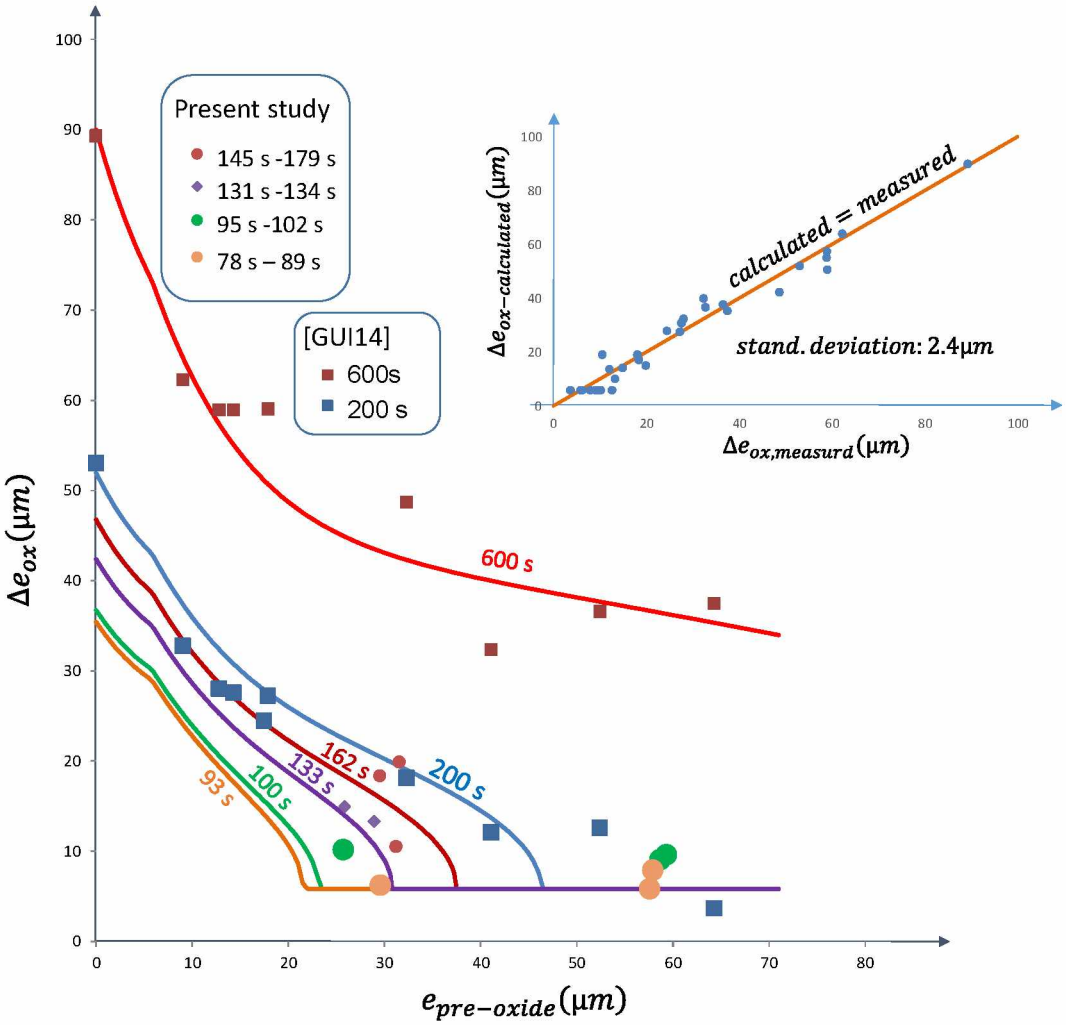

Figure 15: Modeled and measured oxide layer growth at 1200°C versus steam exposure at different pre-oxide layer thicknesses.

The parameters of the model were the following:

$$\delta(\mu m) = Min\left(5.8; 0.56.\, e_{pre-oxide}(\mu m)\right)$$

$$t_D(s) = 4.32.\, e_{pre-oxide}(\mu m)$$

$n = 2$ (i.e. parabolic kinetics),

$$K = 13.5 - 10.8\left(1 - e^{-\frac{e_{pre-oxide}(\mu m)}{8.0}}\right)$$

The delay to initiate high temperature oxidation was found to depend linearly on the pre-oxide layer thickness at 1200°C. This parameter is expected to correspond to the transportation time of oxygen to

cross the entire pre-oxide layer thickness. This suggests that the transport of oxygen at elevated temperature in the pre-oxide layer follows a linear kinetics. This means the process is not diffusion controlled but maybe surface reaction controlled. The kinetic constant, K, was strongly influenced by the thickness of the pre-oxide layer thickness. K was adjusted to also fit the experimental data on as-received bare samples (see [DES16]).

6 Post-Quench mechanical testing and interpretation

6.1 Results

Each oxidized sample was submitted to room temperature tensile testing after the high temperature oxidation. All the mechanical tests failed without developing measurable plastic strains, the tested materials are brittle. The fracture stress extracted from these mechanical tests are given in Table 5, together with the main samples characteristics used to interpret these tests. Because no α(O) inclusions embedded within the prior-β layer were observed (as a result from rather low ECR), the α(O) phase fraction f_α can be directly given by the ratio of the cumulated oxygen enriched α layers thickness (inner and outer sides) to the total metallic layer thickness. The hydrogen in the sample after high temperature oxidation is assumed to be exclusively located in the prior-β phase (see [DES16, DES18]) and directly derived from the hydrogen content after high temperature oxidation and the α-phase fraction. For 1200°C steam oxidation, in spite of some existing scatter, the material fracture stress is controlled by both the hydrogen content within the prior-β phase and the ECR. However, the influence of post-oxidation hydrogen content (see Table.4) is sometimes used in the following as a more straightforward index representing the influence of hydrogen on the mechanical resistance of the samples. The calculation of the fracture stress is described in [DES16, DES18].

Table 5. Main measurements to interpret the samples failure conditions (the grey cells correspond to HT oxidations tests at 1100°C all other were oxidized at 1200°C, simplified test categories are mentioned indicating the pre-oxide layer thickness and the approximate average post-oxidation hydrogen content)

Sample	Test category	ECR_{CP}	$f\alpha$	$[H]_{prior-\beta}$	σ_R
(#)		(%)	(%)	ppm	(MPa)
A_1	30 µm & 270 wppm	13.8	15.4	367	283.0
A_2		14.9	20.7	354	251.4
A_4		12.5	17.2	261	343.9
A_5		11.0	14.2	275	334.5
A_6		9.50	12.6	328	379.3
A_12		12.9	17.2	336	212.4
A_8	60 µm & 500 wppm	10.2	13.1	563	222.2
A_10		11.3	16.2	657	164.7
A_11	30µm & 500 wppm	14.4	20.0	790	270.6
A_13		12.3	16.7	559	224.8

The results are compared to other tests performed on pre-hydrided samples without any pre-oxidation in Figure 16. Considering the test results from [DES16, DES18] eyes-guided splines were drawn showing the trend for several hydrogen contents. For samples containing less than 40 wppm hydrogen, three main fracture modes can be observed on the tests:

- the ductile mode corresponding to samples failing after some plastic deformation. This failure mode was not observed in the scope of this test campaign,

- the brittle failure mode, associated to a fracture stress decreasing with increasing CP-ECR, and attributed to crack nucleation across the brittle layers (zirconia layer and oxygen enriched a-layer) and further propagation through the prior-β layer,

- a fracture mode associated to sample failure without any applied load at very large ECR values.

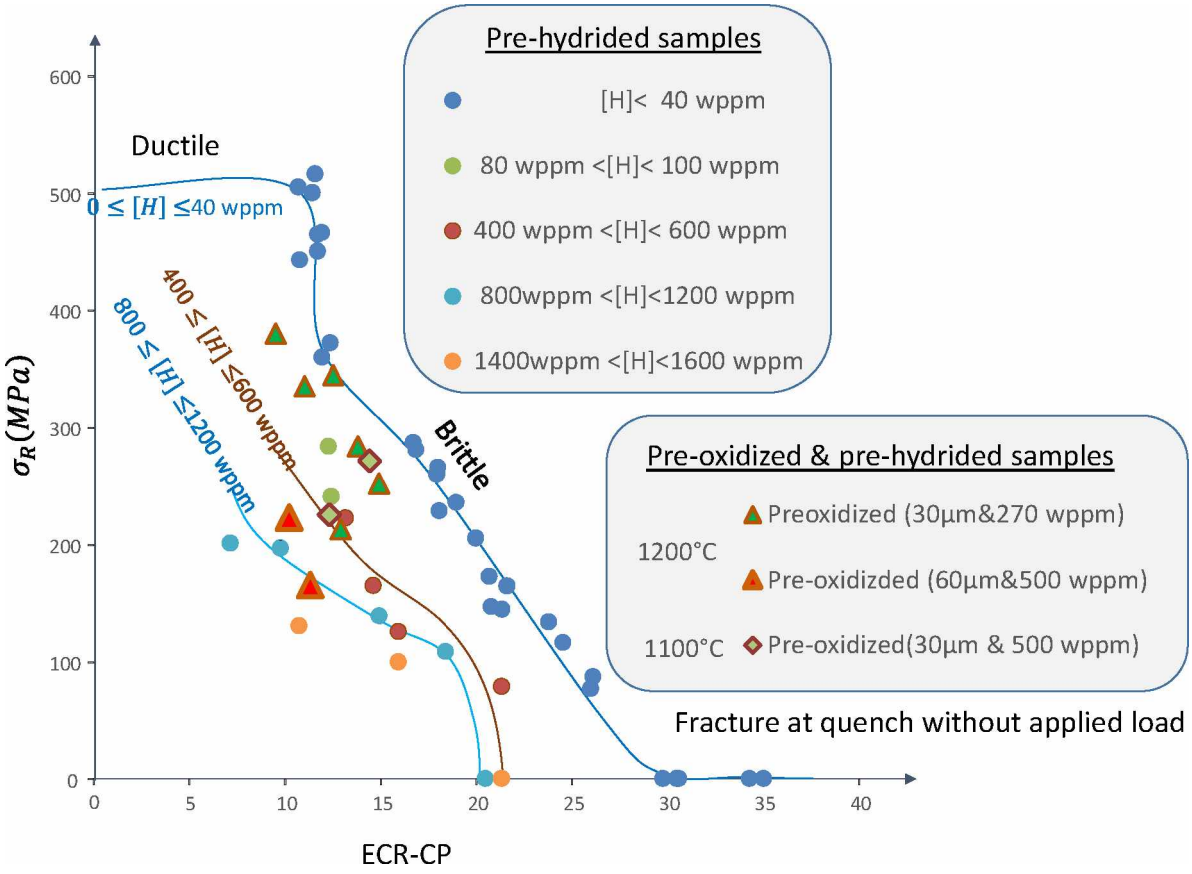

Figure 16: Failure conditions of pre-hydrided [DES16, DES18] and pre-oxidized samples (the hydrogen contents mentioned in the figure are post-HT oxidation values, approximate trends are plotted for each hydrogen content category)

For pre-hydrided samples without any pre-oxidation, the tests performed in [DES16] evidenced a strong decrease of fracture stress with increasing hydrogen content. Regarding samples pre-oxidized and oxidized at 1200°C:

- the 30 µm pre-oxide samples containing about 270 hydrogen wppm (ranging between 216 and 311 wppm and average content of 268 wppm) appear to have a better or comparable resistance with pre-hydrided samples containing 80 to 100 wppm hydrogen,

- the 60 µm pre-oxide samples containing about 500 wppm appear to be more brittle than the 500 wppm pre-hydrided samples, and are rather comparable to the 800 wppm pre-hydrided specimens.

The two tests performed at 1100°C performed on 30 µm thick pre-oxide containing 500 wppm hydrogen show a rather better resistance than the two previous tests at 1200°C with 60 µm pre-oxide and 500 wppm.

There is possibly a specific influence of the pre-oxide layer on the sample fracture condition.

6.2 Linear elastic fracture mechanics analysis

When performing an axial tensile test after a laboratory simulated LOCA, it was already shown [DES16, DES18] that the incipient crack depth best describing the sample brittle failure was the cumulated thickness of zirconia layers and oxygen enriched α phase. We can now extend this crack depth, "a", to a pre-oxidized sample by taking into account the pre-oxide layer, the high temperature formed oxide layer and the oxygen enriched α(O) layer. These quantities can now be evaluated using equations (4) and (5):

$$a = \Delta e_{ox}(\mu m) + e_{preoxide}(\mu m) + e_{\alpha(O)}(\mu m)$$

All the parameters of interest for 1200°C oxidation are already modeled in [DES16, DES18]. In the present study a direct application of the already developed theory to pre-oxidized claddings is made.

The ductile failure of the samples is modeled in an extremely simplified way assuming the following ultimate tensile stress at failure using variability observed when testing as received materials:

$$R_m(MPa) = 627.\aleph(1; 0.05) \qquad (6)$$

$\aleph(a; \sigma)$: is a normal distribution with average value a and standard deviation σ.

A Monte-Carlo simulation was performed assuming several oxidation times randomly distributed to generate CP-ECRs lower than a maximum value. The scatter of the main parameters was taken into account: ultimate tensile stress, fracture toughness, maximum ECR at failure with zero stress. 2500 Monte-Carlo simulations were systematically performed using the algorithm schematically illustrated in Figure 17. Some of the parameters have been determined in previous studies as mentioned in Figure 17. This simulation was validated to reproduce accurately the results of pre-hydrided samples. The results on pre-oxidized samples are illustrated in Figure 18. The simulations represent acceptably well the pre-oxidized samples results. It is expected that the combination of three possible failure modes for high temperature oxidized material remains valid for pre-oxidized materials. The two failure modes corresponding to large ECR values, LEFM and rupture without applied load are rather confirmed by the study. However, the low ECR ductile range was not reached experimentally and the study of the ductile mode would require additional tests and possibly improved modeling.

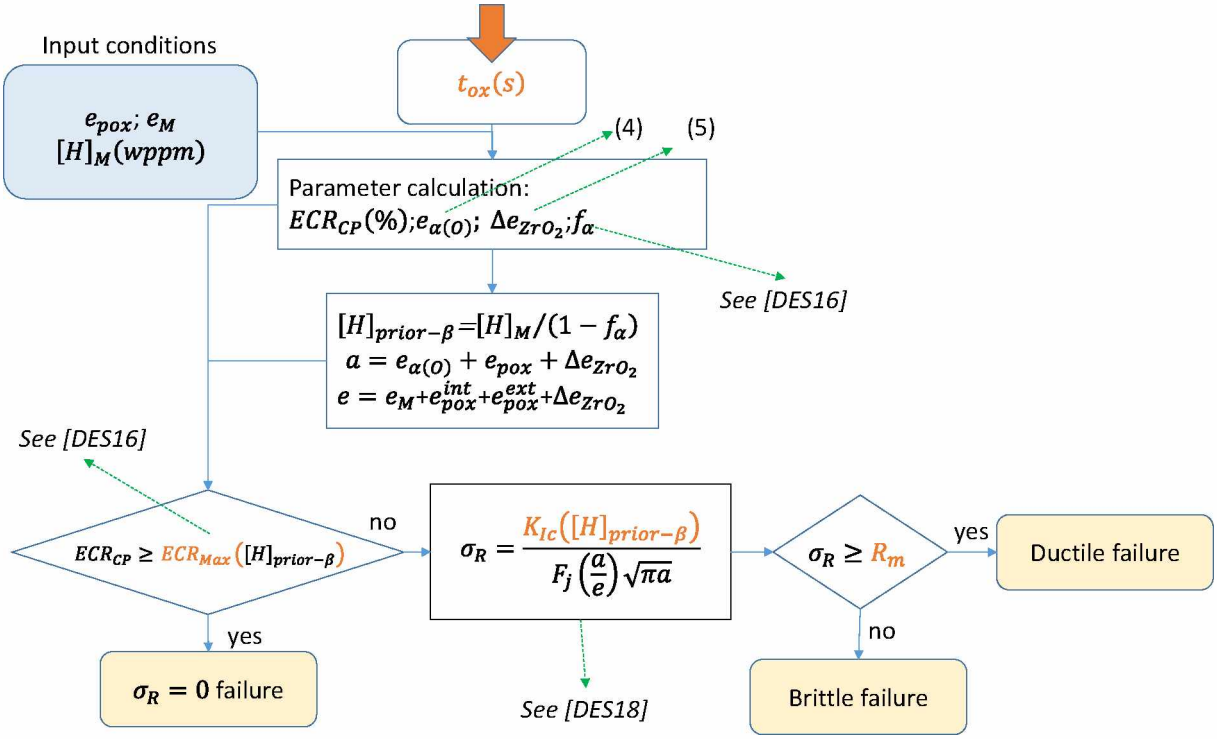

Figure 17: Monte-Carlo simulation scheme.

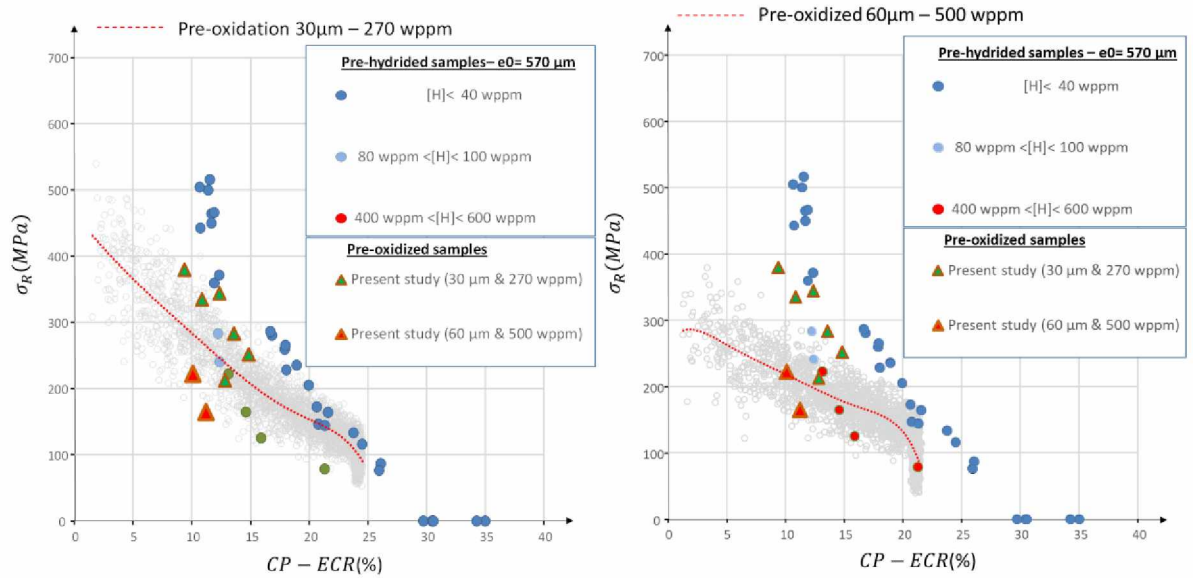

Figure 18: Monte-Carlo simulations (left: 30 µm pre-oxidized samples, right 60 µm pre-oxidized samples – each grey dot represent a simulated condition – the red dotted line represent the average trend of the Monte-Carlo simulation)

7 Conclusion

Some new tests were developed to check the influence of cladding pre-oxidation on post-LOCA quench failure of claddings. The strategy consisted in testing axial tensile samples with well controlled testing conditions and resulted in modeling several aspects of interest:

- influence of a pre-existing oxide scale on high temperature oxidation in laboratory conditions,

- new assessment of the α(O) layer thickness,

- Three combined failure modes are confirmed to describe the entire range of failures of a cladding after a LOCA.

Another key outcome is the weak dependence of α(O) layer thickness on many parameters, such as hydrogen content, the presence of a corrosion layer. On the contrary, the pre-oxide layer appears to have a more complex behavior because of its complex protective influence. Some efforts were made to model the growth of these two layers using laboratory formed pre-oxide. The measurement of α(O) layer thickness requires a lot of care during metallographic preparation whereas the measurement of the oxide layer thickness on metallography is easier. For this reason many strategies to measure the oxygen enriched α(O) layer were developed and compared. The use of well-prepared metallography, fractography, microprobe oxygen profiles show very consistent results. It is finally recommended to use eddy current measurement after high temperature oxidation providing a very accurate assessment of the cumulated thickness of α(O) and zirconia layer. Then it is possible to use a metallograph for an accurate determination of oxide layer thickness and deduce the α(O) layer thickness. The obtained measurements are consistent with Sawarn measurement [SAW16] and Leistikov correlation [LEI87] but rather different from the results expected using the Cathcart-Pawel or Urbanic correlations for this parameter.

This α(O) layer thickness parameter has to be considered as important to interpret experimental data on irradiated material. By comparing the values obtained at several location of a tube, it could be used to evidence temperature gradients in both the axial or azimuthal directions.

It is shown that the post-quench cladding resistance is mainly affected by hydrogen content but also slightly influenced by the presence of a pre-oxide layer. A simple algorithm was developed and extended to pre-oxidized claddings to model the mechanical resistance domain of a cladding sample subjected to a LOCA oxidation transient. The results are rather consistent with experimental data which appears satisfactory.

The developed approach has now to be extended to a ballooned cladding, which would require some more tests on wall-thinned samples to check the influence of ballooning.

Acknowledgements

The content of this paper was technically discussed with Frédérique Rossillon and Antoine Ambard from EDF, resulting in significant improvements. The activity was also financially supported by EDF. Authors also thank the technical team: Stéphane Charbaut, Gaëlle Villevieille, Alice Viretto and Pauline Lacote who made the sample preparation, testing and material characterization.

Appendix

In order to determine the equivalent isothermal transient temperature (T_{ox}), the oxygen enriched α-phase is assumed to grow during the temperature transient measured by the thermocouple T(t) for time varying between t_i and t_f. The end of the transient (t_f) is accurately determined due to the fast cool-down associated to the sample quench.

The α-phase growth is assumed to follow a power-law kinetics : $\frac{d[e_{\alpha(O)}]^n}{dt} = K.e^{-\frac{Q}{RT}}$. In the present study, the Cathcart-Pawel kinetics was used: $e_{\alpha(O)}(\mu m) = \sqrt{2.10^2.0{,}7615e^{-\frac{48140}{1{,}981.T(K)}}.t(s)}$

During the actual transient, the following integral is defined: $I(t_i; t_f) = \int_{t_i}^{t_f} e^{-\frac{Q}{R.T(t)}}dt$

The equivalent isothermal temperature leading to identical oxygen enriched α-layer thickness during t_{ox} (between t_i and t_f) is: $T_{ox} = \frac{Q}{R}\frac{1}{Log\left(\frac{(t_f-t_i)}{I(t_i;t_f)}\right)}$. This temperature only depends on activation energy of the α(O) layer growth kinetics.

The initial time for oxidation period, t_i, is chosen satisfying the condition: $\frac{I(0;t_i)}{I(0;t_f)} < 0.01$. This assumption leads to a measurable but negligible $\alpha(O)$ layer thickness at t_i.

The minimum and maximum temperature, and maximum temperature variation during the equivalent isothermal transient can be determined using the thermocouple temperature record, T(t), as:

$T_{min} = \min_{t\in[t_i;t_f]} T(t)$; $T_{max} = \max_{t\in[t_i;t_f]} T(t)$; $\Delta T = \frac{T_{max}-T_{min}}{2}$

References

[BAK62] L. Baker, L. C. Just, "Studies of metal-Water reactions at high temperature – III Experimental and theoretical studies of the zirconium-water reaction", ANL-6548, 1962.

[BOS06] P. Bossis, D. Pêcheur, K. Hanifi, J. Thomazet, M. Blat, "Comparison of the High Burn-Up Corrosion on M5 and Low Tin Zircaloy-4", Journal of ASTM International, January 2006, Vol. 3, No. 1 - Paper ID JAI12404.

[BOU15] S. Boutin, S. Graff, "A new LOCA safety demonstration in France", Top Fuel meeting, 13-17 September 2015.

[BRA08] J.-C. Brachet, V. Vandenberghe-Maillot, L. Portier, D. Gilbon, A. Lesbros, N. Waeckel, J.-P. Mardon, "Hydrogen Content, Preoxidation, and Cooling Scenario Effects on Post-Quench Microstructure and Mechanical Properties of Zircaloy-4 and M5® Alloys in LOCA Conditions", Journal of ASTM International, Vol. 5, No. 5. Paper ID JAI101116.

[BRA12] I. V. Branzoi, M. Iordoc, F. Branzoi, G. Rimbu, "Growth and characterization of zirconia ceramic film formed by plasma electrolytic oxidation on biomedical Zr3Ta alloy", Surface and Interface Analysis, vol. 12, pp. 914-918, 2012.

[CAB15] A. Cabrera, N. Waeckel, "A strength based approach to define LOCA limits", Top Fuel meeting, 13-17 September 2015.

[CAT77] J.V. Cathcart, R.E. Pawel, R.A. McKee, R.E. Druschel, G.J. Yurek, J.J. Campbell, S.H. Jury, « Zirconium metal-water oxidation kinetics – IV Reaction rate studies », ORNL/NUREG/17, August 1977.

[CHU77] H. M. Chung, T.F. Kassner, "Pseudo-binary Zircaloy-oxygen phase diagram", Journal of Nuclear Materials, Volume 84, October 1979, Pages 327-339.

[DES16] J. Desquines, D. Drouan, S. Guilbert, P. Lacote, « Embrittlement of pre-hydrided Zircaloy-4 by steam oxidation under simulated LOCA transients", Journal of Nuclear Materials, Volume 469, February 2016, Pages 20-31.

[DES18] J. Desquines, S. Guilbert, T. Taurines, V. Busser, « Fracture mechanics analysis of Zircaloy-4 tubular samples after laboratory simulated LOCA transients", Engineering Fracture Mechanics, vol.193, pp. 96-107, 2018.

[DUR19] C. Duriez, O. Coindreau, M. Gestin, A. Kasperski, M. Mermoux, « Zircaloy-4 high temperature oxidation in atmospheres representative of SFP-LOCA: Investigation of the influence of a low temperature pre-oxidation scale", Journal of Nuclear Materials, Volume 513, January 2019, Pages 152-174.

[GRO12] M. Große, M. van den Berg, G. Goulet, A. Kaestner, "In-situ investigation of hydrogen diffusion in Zircaloy-4 by means of neutron radiography", Journal of Physics: Conference Series 340(2012) 012106 - doi:10.1088/1742-6596/340/1/012106.

[GUI14] Guilbert, S., Lacote, P., Montigny, G., Duriez, C., Desquines, J., and Grandjean, C., "Effect of Pre-Oxide on Zircaloy-4 High-Temperature Steam Oxidation and Post- Quench Mechanical Properties," Zirconium in the Nuclear Industry: 17th International Symposium, STP 1543, Robert Comstock and Pierre Barberis, Eds., pp. 952–978, doi:10.1520/STP154320120166, ASTM International, West Conshohocken, PA 2014.

[GUI16] S. Guilbert-Banti, J. Desquines, "Fuel Cladding post-quench LOCA Embrittlement: Mechanical test Relevance", Top Fuel 2016, Boise, ID, September 11-15, 2016.

[HON01] K. Honma, S. Doi, M. Ozawa, S. Urata, T. Sato, "Thermal-shock behavior of PWR high burnup fuel cladding under simulated LOCA conditions", ANS 2001 Annual Meeting, Milwaukee, Wisconsin, USA, June 17-21 (2001).

[KAS18] A. Kasperski, C. Duriez, M. Mermoux. 2018. «Combined Raman Imaging and ^{18}O Tracer Analysis for the Study of Zircaloy-4 High-Temperature Oxidation in Spent Fuel Pool Accident». In Zirconium in the Nuclear Industry: 18th International Symposium, ASTM International.

[KIM06] J. H. Kim, B. K. Choi, J. H. Baek, Y. H. Jeong, "Effects of oxide and hydrogen on the behavior of Zircaloy-4 cladding during the loss of the coolant accident (LOCA)", Nuclear Engineering and Design 236 (2006) 2386–2393.

[LEI83] S. Leistikov, G. Schantz, H. V. berg, A. E. Aly, "Comprehensive presentation of extended Zircaloy-4 steam oxidation results 600-1600°C", PCDE-NEA-CSNI/IAEA Specialists' Meeting on Water Reactor

Fuel Safety and Fission Products Release in Off-Normal and Accident Conditions, Riso National Laboratory (Denmark), 16-20 May, 1983.

[LEI87] S. Leistikov, G. Schantz, "Oxidation kinetics and related phenomena of Zircaloy-4 fuel cladding exposed to high temperature steam and hydrogen-steam mixtures under PWR accident conditions », Nuclear Engineering and Design, vol. 103, (1987), p.p. 65-84.

[LES19] M. Le Saux, J.-C. Brachet, V. Vandenberghe, S. Urvoy, A. Ambard, R. Chosson, « Effect of a pre-oxide on the high temperature steam oxidation of Zircaloy-4 and M5FRAMATOME alloys », Journal of Nuclear Materials 538 (2019), p.p. 386 – 399.

[LEE19] C.M. Lee, Y.S. Han, Y.K. Mok, D.S. Sohn, "Study of mechanism of oxidation resistance enhancement induced by preformed oxide on zirconium alloys", Corrosion Science 158 (2019) 108105.

[MAK76] H. Maki, M. Ooyama, "Behavior of Zircaloy fuel cladding tubes", Journal of Nuclear Science and Technology, vol. 13, issue 2, pp.43-57, 1976.

[NAG04] F. Nagase, T. Fuketa, "Effect of pre-hydriding on thermal-shock resistance of Zircaloy-4 cladding under simulated loss-of-coolant conditions", Journal of Nuclear Science and Technology, vol. 41, n°7, pp. 723-730 (2004).

[NAG05] F. Nagase, T. Fuketa, "Behavior of pre-hydrided Zircaloy-4 cladding under simulated LOCA conditions", Journal of Nuclear Science and Technology, vol. 42, n°2, pp. 209-218 (2005).

[NAG06] F. Nagase, "Fracture behavior of irradiated Zircaloy-4 cladding under simulated LOCA conditions", Journal of Nuclear Science and Technology, vol. 43, n°9, pp. 1114-1119 (2006).

[NAG09] F. Nagase, T. Chuto, T. Fuketa, "behavior of high burnup fuel cladding under LOCA conditions", Journal of Nuclear Science and Technology, vol. 46, n°7, pp. 763-769 (2009).

[NAG10] F. Nagase, "Status and plan of LOCA studies at JAEA", Fuel Safety Research Meeting, May 19-20 2010, Tokai, Japan (2010).

[NAR19] T. Narukawa, M. Amaya, "Behavior of high-burnup advanced LWR fuel cladding tubes under LOCA conditions", Topfuel 2019 conference, September 22-26, 2019, Seattle Washington USA.

[SAW16] T. K. Sawarn, Suparna Banerjee, S. Kumar, "Study of the response of Zircaloy- 4 cladding to thermal shock during water quenching after double sided steam oxidation at elevated temperatures", Journal of Nuclear Materials 473 (2016) 237-248.

[THI19] R. Thieurmel, J. Besson, E. Pouillier, A. Parrot, A. Ambard, A.-F. Gourgues-Lorenzon, "Contribution to the understanding of brittle fracture conditions of zirconium alloy fuel cladding tubes during LOCA transient", Journal of Nuclear Materials 527 (2019).

[URB78] V.F. Urbanic, T.R. Heindrick, "High temperature oxidation of Zircaloy-2 and Zircaloy-4 in steam", Journal of Nuclear Materials 7.5 (1978) 251-261.

[VRT05] V.Vrtílková, L.Novotný, V.Hamouz, R.Doucha, "Practical illustration of the traditional versus alternative LOCA embrittlement criteria", International Conference, Nuclear Energy for New Europe 2005, Bled, Slovenia, September 5-8, 2005.